Feature-resolved computational and analytical study of laminar drag reduction by superhydrophobic surfaces

Yixuan Li, Karim Alame, and Krishnan Mahesh[*]
Department of Aerospace Engineering and Mechanics, University of Minnesota,
Minneapolis, Minnesota 55414, USA
(Received 1 February 2017; published 23 May 2017)

Direct numerical simulations are used to study the drag reduction by superhydrophobic surfaces in laminar channel flow. Resolved multiphase simulations using the volume of fluid methodology are performed to study the effects of groove geometry, interface shear rate, and meniscus penetration independently. An analytical solution for the flow in a laminar channel with a grooved surface with a gas pocket within is obtained. The solution accounts for both the groove geometry and the trapped fluid properties, and shows good agreement with simulation results. The solution is used to propose a scaling law that collapses data across fully wetted to fully gas-filled regimes. The trapped gas is simulated as both flat and meniscal interfaces. The drag reduction initially increases with interface deflection into the groove and then decreases for large deflections as the interface velocity approaches zero due to the proximity to the bottom of the groove.

I. INTRODUCTION

Superhydrophobicity is the property wherein surfaces can maintain large contact angles for sessile drops, thereby exhibiting low wettability; such a state is called the Cassie-Baxter state [1]. The superhydrophobic effect has been attributed to both surface chemistry and roughness. The trapped gas layer has been hypothesized to lower the shear at the interface, thus reducing drag on the surface. This observation has inspired several investigators to study such surfaces for their application to drag reduction in both laminar and turbulent flows (see recent reviews in [2–5] and references therein).

The most common assumption in theoretical analysis and simulations (e.g., [6–12]) in the superhydrophobic surfaces (SHSs) context is that the gas-liquid interface is flat and shear free. Early theoretical work by Philip [13,14] obtained the solution of a laminar channel flow with alternating no-slip and no-shear boundary conditions on one wall, using conformal mapping. These results have been widely applied to superhydrophobic surfaces. Lauga and Stone [15] further extended this solution to pipe flow. The effect of orientation of the strips on the overall drag reduction was investigated, and the effective slip length for longitudinal strips has been shown to be twice that for transverse strips with the same coverage ratio. More importantly, it is proposed that the effective slip length is shear dependent. And the shear-independent slip length can be a limit of more general slip behavior. Another extension of [13] is the analytical solution by [16], which contains the viscosity ratio of two fluids by assuming an approximate local slip length as a function of the groove aspect ratio at the interface. Belyaev and Vinogradova [17] described the interface with a prescribed constant local slip length in order to apply the "gas cushion" model [18]. Nizkaya *et al.* [19] generalized this model to include the viscosity ratio and the geometry of the surface using the operator method. Busse *et al.* [20] took the dissipation of the air-water layer into consideration, but neglected the geometric features of the surface. The dissipation at the interface is included in [21] by coupling between the liquid channel flow and trapped gas pocket. The interface is assumed to be flat and the gas to flow as a convection cell. This coupled liquid-gas prediction lies between the zero shear

---

*kmahesh@aem.umn.edu

model and the experiments. One conjecture of the discrepancy between the experimental data and coupled liquid-gas model is that the shape of the meniscus is not flat. In the comparison of the slip length between the molecular-dynamics simulation and a semianalytical solution of SHSs in strips, Cottin-Bizonne *et al.* [22] also have suggested that the shape of the interface is important when normal pressure is increased.

The meniscus shape has been the subject of many recent studies. Sbragaglia and Prosperetti [23] used perturbation methods to calculate the correction to the effective slip length due to small interface curvature. Extensions of this work to large interface curvature regime include [24], who used a finite element solver to solve for the effective slip length; and [25] who used conformal mapping. Reference [26] used conformal mapping to study transverse flow passing an array of bubbles. However, these three studies assumed the interface to be shear free, therefore resulting in a positive monotonic increase of the slip length with respect to increasing contact angle (from protruding out of the gas to into the gas). The same trend is found in the numerical results in [7]. This trend is inconsistent with the molecular-dynamics simulations conducted by [22,27], showing that there is a preferential normal pressure or contact angle (protruding into the gas) to achieve an optimum slip length between the normal and the superhydrophobic state. Similarly, in the study of the dynamical property of the interface in [28], it is found that the effective slip length is very sensitive to the penetration of the meniscus into the groove. Such a nonmonotonic trend is also observed in the present paper.

The sustainability of the air pocket is another important issue. In an experiment of a turbulent Taylor-Couette flow with SHSs by Rosenberg *et al.* [29], patches of the air-impregnated surface failed, yielding a Wenzel state. The liquid-infused surface with a viscosity ratio of $\mu_{\text{ext}}/\mu_{\text{int}} \sim O(1)$ performed better than the air-infused interface. The drainage problem of liquid-infused surface has been studied in [30]. One main reason for the failure of the air pocket is that it comes in contact with the bottom of the groove [31]. Such a state is described as a criterion of the meniscus radius $R_{\text{cr}} \sim w^2/b$ (w and b are the cavity width and depth respectively) in [32,33]. In addition to this geometrical threshold, the balance of force between surface tension and the pressure across the interface is studied in [34–36]. The maximum pressure to sustain the interface for a grooved surface is given by

$$\Delta p \leqslant -2\sigma \cos\theta/[(w+d)\phi], \tag{1}$$

where σ is the surface tension of a liquid, θ is the contact angle of the liquid on the solid surface, ϕ_g is the gas fraction, and $(w+d)$ is the groove spacing.

When the interface fails, water penetrates into the surface, and the grooves become fully wetted. Kamrin *et al.* [37] have derived a second-order accurate matrix to describe the effective slip boundary condition of a laminar shear flow at the mean surface height of an arbitrary periodic surface. Wang [38] solved the shear flow over longitudinal or transverse grooves using eigenfunction expansions and matching. [39] studied the partially wetted grooves problem but assuming an infinite slip boundary condition at the interface. Here, we study the general problem of partially filled grooves using theory and simulations. The solution of the effective slip length can be used *a priori* as a scaling factor to predict the drag reduction. We use the scaling law of effective slip length predicted by [40] with respect to interface coverage ratio to validate our result.

In this work, we explore the drag reduction features of SHSs using direct numerical simulations (DNSs) and volume of fluid (VOF) simulations. An analytically obtained scaling law for drag reduction is proposed. The VOF simulation is used as a benchmark to conduct controlled studies of two commonly omitted components: gas flow and penetration. In Sec. II B the VOF method is validated against the experiment by Maynes *et al.* [21] and evaluates the effects of gas flow and penetration of the interface. In Sec. III, an analytical solution is obtained that accounts for groove geometry as well as properties of both fluids. The analytical solution is compared to the VOF simulation and DNS results and used to develop a scaling law for the effective slip length which collapses data across fully wetted to fully gas-filled regimes (Sec. III C). The effect of interface

curvature is studied in Sec. IV by describing the interface with the Young-Laplace equation. The conclusions of this work are summarized in Sec. V.

II. METHODOLOGY

A. Computational method

Direct numerical simulations (DNSs) are performed using a mass conserving VOF methodology on structured grids to study the gas-liquid interface within a groove. The governing equations are solved using the finite volume algorithm developed by Mahesh *et al.* [41] for solving the incompressible Navier-Stokes equations on unstructured grids. The algorithm emphasizes discrete kinetic energy conservation in the inviscid limit which enables it to simulate high-Reynolds number flows in complex geometries without adding numerical dissipation. The solution is advanced using a predictor-corrector methodology where the velocities are first predicted using the momentum equation alone, and then corrected using the pressure gradient obtained from the Poisson equation yielded by the continuity equation. The time advancement is implicit and uses the Crank-Nicholson discretization with a linearization of the convection terms.

The volume fraction is represented by a color function c to keep track of two different fluids. The function c varies between the constant value of 1 in a full cell to 0 in an empty cell, with an intermediate value between 0 and 1 to define an interface cell. The volume of each fluid cell is tracked in a two-step process for each time iteration: the reconstruction and advection steps. The reconstruction step is based on a set of analytic relations proposed by [42]; given the volume fraction in each cell, the reconstruction of the interface shape uses a local normal vector and a piecewise linear interface calculation (PLIC) to approximate the interface shape. This step geometrically conserves the volume in each cell and therefore conserves mass and prevents over- and undershoots in the value of the color function, which ensures boundedness. The color function is then advected with the fluid velocity field, while geometrically conserving the area using a directionally split flux scheme to exchange the reference phase volume across the boundary of neighboring cells.

The governing equations are given by the color function material derivative, momentum, and continuity equations:

$$\frac{\partial c}{\partial t} + u_j \frac{\partial c}{\partial x_j} = 0, \tag{2}$$

$$\frac{\partial u_i}{\partial t} + \frac{\partial}{\partial x_j}(u_i u_j) = -\frac{1}{\rho}\frac{\partial p}{\partial x_i} + \frac{1}{\rho}\frac{\partial}{\partial x_j}\left[\mu\left(\frac{\partial u_i}{\partial x_j} + \frac{\partial u_j}{\partial x_i}\right)\right] + F_{st,i} + K_i, \tag{3}$$

$$\frac{\partial u_i}{\partial x_i} = 0. \tag{4}$$

In Eq. (2) we have c as the color function that represents the fluid in each phase in the VOF methodology, u_i and x_i are the ith component of the velocity and position vectors respectively. In Eq. (3), p denotes pressure, ρ is density, and μ is viscosity of the fluid. The fluids are assumed to be immiscible. Hence, the density and viscosity are evaluated as

$$\rho = \rho_2 + (\rho_1 - \rho_2)c, \tag{5}$$

$$\mu = \mu_2 + (\mu_1 - \mu_2)c. \tag{6}$$

Additionally in Eq. (3) we have K_i as the body force and $F_{st,i}$ as the surface tension force, which is modeled as a continuum surface force as proposed in [43]:

$$F_{st,i} = \sigma \kappa \frac{\partial c}{\partial x_i}, \tag{7}$$
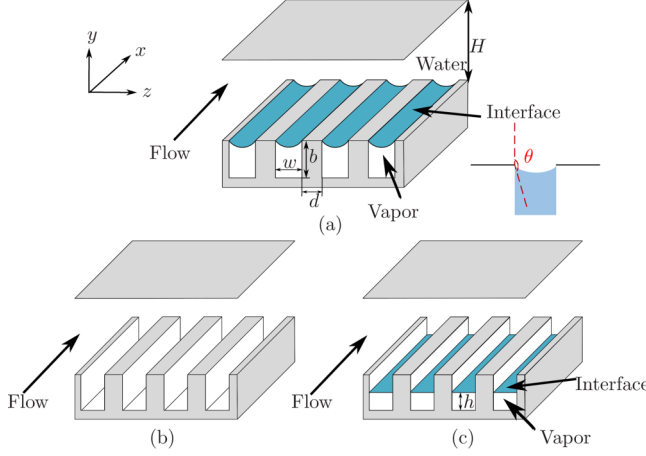
FIG. 1. The channel geometry and groove configuration. (a) Grooved channel with meniscus interfaces (cases M7, M12, and M25). Definition of the contact angle θ in this paper is shown on the right. (b) Fully wetted grooved channel (cases F7, F12, and F25). (c) Grooved channel with flat interfaces (cases I7, I12, and I25).

where σ is the surface tension constant, and κ is the curvature calculated using the height function which has been shown to significantly reduce numerical errors that are associated with surface tension. These errors are known as spurious currents [44]. The gradient of the color function is given by $\frac{\partial c}{\partial x_i}$ and is representative of the surface normals. The gradient term in the surface tension force is discretized in the same manner as the pressure gradient term in the projection step:

$$\Delta t \sum_f \frac{\partial p}{\partial N} A_f = \sum_f \hat{v}_N A_f + \Delta t \sigma \kappa \sum_f \frac{\partial c}{\partial N} A_f, \tag{8}$$

where N denotes the outward normal of face with respect to the control volume, on which the summation is carried out. This method of discretization ensures proper pressure jump recovery across the interface.

In a channel with smooth walls, the friction factor is $f = f(\text{Re})$ for laminar flow. As Fig. 1 shows for a channel with SHSs, the independent variables are H, w, d, b, h, $\mu_{\text{gas}}/\mu_{\text{liquid}}$, $\rho_{\text{gas}}/\rho_{\text{liquid}}$, $\dot{Q}_{\text{liquid}}$, σ, g, where H is the height of the channel, w is groove width, d is the distance between the grooves, b is the groove depth, $\mu_r = \mu_{\text{gas}}/\mu_{\text{liquid}}$ is the liquid to gas viscosity ratio, $\rho_{\text{liquid}}/\rho_{\text{gas}}$ is the liquid to gas density ratio, $\dot{Q}_{\text{liquid}}$ is the volume flow rate of the liquid, σ is the surface tension of the gas-liquid interface, g is the gravitational acceleration. Nondimensionalization yields the friction factor $f = f[\text{Re}, \mu_r, \rho_{\text{liquid}}/\rho_{\text{gas}}, w/(w+d), H/(w+d), h/b, b/H, \text{We}, \text{Bo}]$, where $\text{Re} = \rho_{\text{liquid}} U(w+d)/\mu_{\text{liquid}}$, $\text{We} = \rho_{\text{liquid}} U^2(w+d)/\sigma$, $\text{Bo} = (\rho_{\text{liquid}} - \rho_{\text{gas}})g(w+d)^2/\sigma$, $U = Q/A$. The density and viscosity ratio are constants. The governing parameters for a channel with SHS are the coverage ratio $\phi = w/(w+d)$, and the channel aspect ratio $H/(w+d)$. Accounting for groove geometry and interface surface tension introduces the additional parameters above. Different models are simulated numerically to conduct a thorough study of the factors that contribute to drag reduction. The simulation parameters are listed in Table I. Case number prefixes "F," "I," and "M" represent fully wetted, interface, and meniscus studies. The cross section configuration is shown in Fig. 1.

The simulations were performed at a constant liquid flow rate, which defines the drag reduction as

$$\text{DR} = \frac{K_{\text{no-slip}} - K_{\text{SHS}}}{K_{\text{no-slip}}}, \tag{9}$$

TABLE I. Simulation parameters. Case number prefixes F, I and M represent fully wetted, interface, and meniscus studies. The depth of the groove is fixed at $b/(w + d) = 0.625$. $Re = 4 \times 10^{-4}$.

	Case	$H/(w + d)$	ϕ	$h/b(\%)$	$Bo(\times 10^{-4})$	$We(\times 10^{-3})$
Fully wetted	F7	1.88	1/4, 1/2, 3/4	n/a	n/a	n/a
	F12	3.1875	1/4, 1/2, 3/4	n/a	n/a	n/a
	F25	6.25	1/4, 1/2, 3/4	n/a	n/a	n/a
Flat interface	I7	1.88	1/4, 1/2, 3/4	28, 60, 90, 100	n/a	n/a
	I12	3.1875	1/4, 1/2, 3/4	28, 60, 90, 100	n/a	n/a
Flat interface	I25	6.25	1/4, 1/2, 3/4	28, 60, 90, 100	n/a	n/a
	M7	1.88	1/2	n/a	2.22	5.56
Meniscus	M12	3.1875	1/2	n/a	2.22	5.56
	M25	6.25	1/2	n/a	2.22	5.56

where $K_{\mathrm{no-slip}}$ and K_{SHS} are the body force applied to the no-slip or SHS channel respectively. Periodic boundary conditions are imposed in the streamwise and spanwise directions. The grid size is, e.g., for F7 $N_x \times N_y \times N_z = 3 \times 151 \times 161$ for the channel part, and $N_x \times N_y \times N_z = 3 \times 61 \times 81$ to resolve the groove. Grid convergence studies were performed. Doubling the number of nodes in z and y for the case F7 ($\phi = 1/2$) changed the body force by only 0.02%. Similarly, for the VOF case involving a flat or a meniscus interface, the grid size was refined until the drag reduction difference was less than 1%.

B. VOF validation

In this section, the VOF solver is validated with the analytical solutions in [20] and the effect of gas flow assumption is evaluated by simulating the experiment in [21]. After liquid penetration is considered, the VOF solver shows good agreement with the experiment data.

1. Gas flow effect on interface shear

The effect of gas flow can be evaluated for canonical channel flow with liquid and gas phases separated by a flat interface (Fig. 2). Two different assumptions can be made for the flow in the gas layer, as has been discussed in [20]. The first assumption is that the same pressure gradient acts as in the liquid layer (realized in experiment [45] by constant injection of gas). The second assumption is enforcing the mass flow rate of the gas layer to be zero (realized in experiment by grooves with capped ends to entrap the gas), which induced a reverse flow inside the gas layer. A third possibility is zero pressure gradient in the gas layer, i.e., the gas layer is driven by the outside liquid layer,
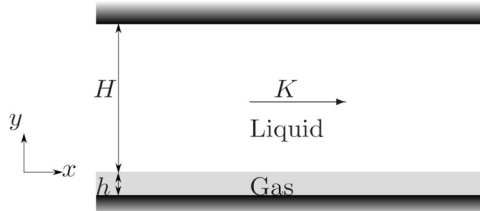

FIG. 2. Schematic diagram of a fully developed laminar channel with stable gas-liquid interface. Flow direction is from left to right. H is the height of the channel; h is the height of the gas layer; K is the body force.
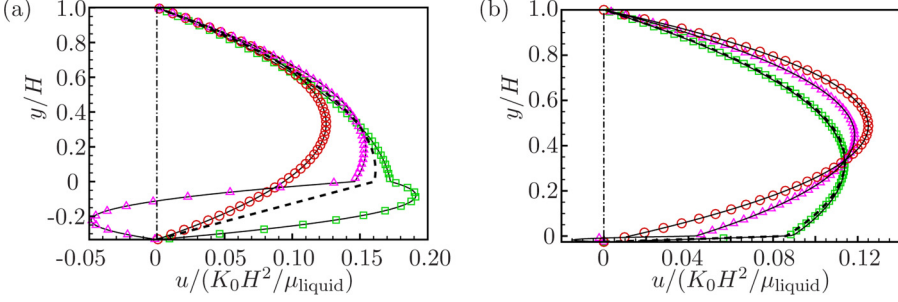
FIG. 3. Comparison of the velocity profiles in a flat channel with a gas layer thickness ratio of (a) $h_r = 0.33$ and (b) $h_r = 0.026$. The viscosity ratio is $\mu_r = \mu_{gas}/\mu_{liquid} = 0.02$. Symbols are the VOF simulations ($\bigcirc$ no gas layer, $\square$ equal pressure gradient in both phases, $\triangle$ zero volume flow rate in gas layer). Solid line (——) is for the analytical solutions in [20]. Dashed line (— —) is the analytical solution in Eqs. (10) and (11).

therefore acting as a Couette flow. And the analytical solutions for $u(y)$ in both phases are

$$u_{liquid} = -\frac{y^2}{2} + \frac{\mu_r}{2(\mu_r + h_r)}y + \frac{h_r}{2(\mu_r + h_r)}, \qquad (10)$$

$$u_{gas} = \frac{1}{2(\mu_r + h_r)}(y + h_r), \qquad (11)$$

where $\mu_r = \mu_{gas}/\mu_{liquid}$, $h_r = h/H$ is the normalized height of the gas, and velocities are normalized by KH^2/μ_{liquid}.

Simulations were performed for two limiting values of gas layer height ratio, $h_r = h/H = 0.026$ and 0.33 with constant flow rate and the two different gas flow assumptions. The velocity profiles of VOF simulation agree with the analytical solutions obtained in [20] with the two gas layer conditions. Examining Figs. 3(a) and 3(b), the main observable difference is the effect of gas flow on the interface. When the gas layer is large, the gas layer assumptions show an obvious difference: the pressure gradient assumption produces a Poiseuille flow component to the gas. However when the layer is thin enough, the Couette flow assumption collapses with the pressure gradient assumption, which suggests an approximate boundary condition to represent the gas-liquid interface:

$$\frac{du_{gas}}{dy} \sim \frac{u_{gas}}{h}, \quad \text{yielding} \quad \frac{du_{liquid}}{dy} \approx \mu_r \frac{u_{liquid}}{h_r}. \qquad (12)$$

This is accurate in a Couette type gas flow and also representative of a pressure driven gas flow when the gas layer is thin. Note that one can rework Eqs. (2) and (3) in [19] and get the same expression.

Next, the experiment conducted in [21] was simulated by VOF numerically. In the experiment, the channel has varying groove widths on the top and bottom walls. The drag reduction is quantified in terms of the Darcy friction factor–Reynolds number product $f\text{Re}$ as a function of groove widths nondimensionalized by the total pitch length (sum of rib and cavity widths). A channel ($H = 7.69$, $w + d = 4$) flow with grooves ($b = 2.5$) on both walls was simulated by assuming three different gas flow conditions: equal pressure gradient in both phases; zero volume flow rate inside the groove; zero pressure gradient inside the groove. The gas was assumed to fill the entire groove and the interface was flat. Inside the grooves, under different gas flow conditions, the gas behaves differently as shown in Fig. 4. Similar to Fig. 2, under equal pressure gradient, the gas flow has a Poiseuille flow component, generating a large slip velocity at the groove top. But in Figs. 4(b) and 4(c), the magnitude of the slip velocity generated by the gas flow is close, although a reverse flow is produced inside the groove when the volume flow rate of gas is enforced to be zero. Figure 5 shows the comparison of the Darcy friction factor–Reynolds number product $f\text{Re}$ determined from the expression $f\text{Re} = 2/\bar{U}$, where $\bar{U}$ is the average velocity normalized by $4KH^2$. In Fig. 5, the equal pressure gradient in both phases yields the least amount of drag, similar to what was observed for the
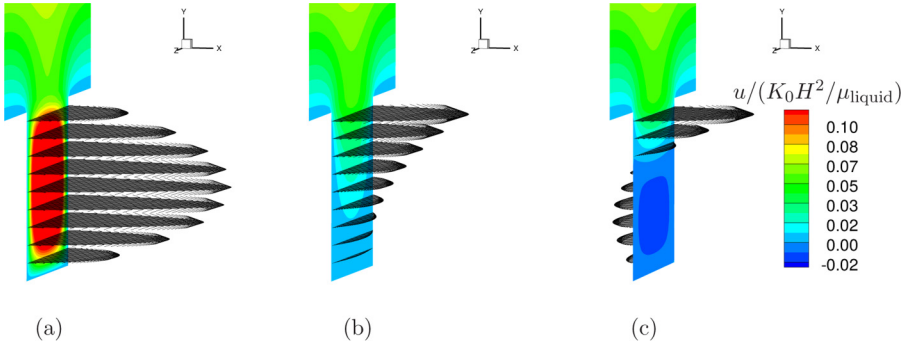
(a)   (b)   (c)

FIG. 4. Vector plots inside the grooves of the same grooved channel $\phi = 0.5$, $H = 7.69$, $w + d = 4$, $b = 2.5$ with different gas flow conditions. Backgrounds are contour plots of streamwise velocity. (a) Equal pressure gradient in both phases. (b) Zero pressure gradient inside the groove. (c) Zero volume flow rate inside the groove. The vector length has been rescaled for plotting purpose.

canonical multiphase channel. Both the zero pressure gradient and the zero volume flow rate cases are very close but the latter still has higher drag. All three cases predict the same trend as experiments. The recirculating gas flow is the closest; the levels however are lower than the experiments. This behavior is similar to the trend observed by the cavity model of Maynes *et al.* [21]. They speculate that the difference is because change of streamwise pressure induces a continuous change on the meniscus shape that eventually causes the liquid to penetrate slightly into the groove, thus reducing the effective gas layer height.

2. Liquid penetration effect

In order to quantify the effect of the meniscus penetration, in this section, a solid-gas contact angle $\theta = 150°$ (defined in Fig. 1) is prescribed. The contact angle is identical to the surface property reported in the experiment of [21]. The obtained results are shown in Fig. 6(a). It is clear that for the same gas flow condition, the flat interface underpredicts the friction, but when a meniscus shape is introduced, the results match well with experiment. This implies that the meniscus shape which draws liquid into the groove has a more appreciable effect on drag reduction as compared to the gas flow condition.
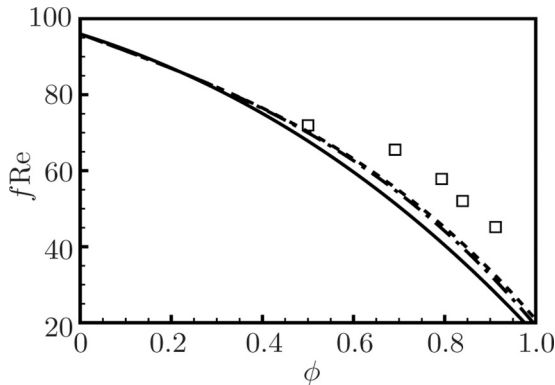

FIG. 5. Comparison of $f\mathrm{Re}$ with varying groove fractions ϕ ($\square$ experimental results in [21], ── for equal pressure gradient in both phases, ── for zero volume flow rate inside the groove, ·── for zero pressure gradient inside the groove).

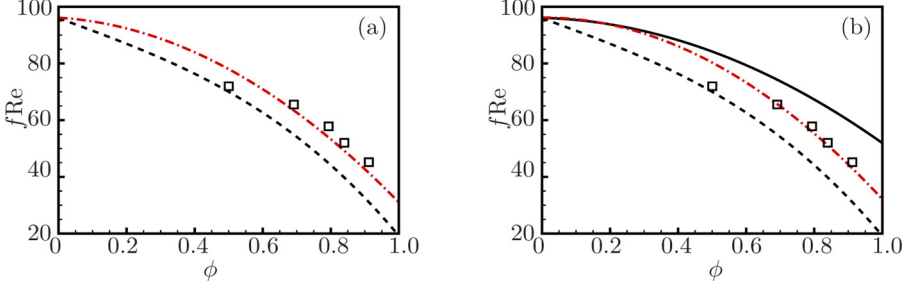FIG. 6. Comparison of $f\mathrm{Re}$ with varying groove fractions ϕ. (a) $\cdot\!-$ meniscus shape of contact angle $150°$; (b) $\cdot\!-$ flat interface with 16% water penetration, $-\!-$ for a fully wetted groove ($\square$ experimental results by Maynes *et al.* [21], $\cdot \cdot \cdot$ for full gas pocket filling the groove).

To test this notion and to find a flat interface representative of the liquid penetration, three simulations with different gas-liquid setups are tested: (i) flat gas-liquid interface with gas filling the entire groove; (ii) flat gas-liquid interface with the liquid filling 16% of the groove; and (iii) liquid filling the entire groove.

The 16% liquid penetration is selected so that the volume of fluid penetrating into the groove is the same as applying a meniscus with a contact angle $\theta = 150°$. The grooves are supposed to be capped at the end, i.e., zero flow rate is imposed inside the grooves. Figure 6(b) shows the results obtained from the three cases. Case (i) underpredicts the drag. Case (ii) where the liquid penetrates 16% into the groove matches the experiment data whereas case (iii) with the groove being fully wetted overpredicts the drag. It can be concluded that the geometry by itself has an effect on overall drag reduction, and liquid penetrating into the groove also affects the overall drag.

III. ANALYTICAL SOLUTION

A. Model problem

The influence of liquid penetration observed in Sec. II B leads us to derive an analytical solution that accounts for its effect. Typically, the texture size of SHSs in turbulent experiments in viscous units $(w + d)^+ = u_\tau L/\nu < 5$ [46,47]. When the groove is relatively small to the channel, the flow in the vicinity of the grooves can be treated as shear flow. The shear-driven flow over longitudinal grooves with coupled gas-liquid interface within the grooves can be solved analytically as follows. A corresponding solution for fully wetted groove solutions is obtained by [38], which can be recovered from the current solution using asymptotic analysis (see the Appendix).

The model problem is illustrated in Fig. 7. The flow is normal to the (y,z) plane, and the streamwise velocity u is normalized by $(L\tau/\mu)$. All lengths are normalized by L, where L is half of the period of the grooves. $a = \phi = w/(2L)$ is half width of the groove. g is the depth of the gas pocket inside the groove. $f + g$ is the depth of the groove. The governing equation is the Laplace equation:

$$\frac{\partial^2 u}{\partial y^2} + \frac{\partial^2 u}{\partial z^2} = 0. \tag{13}$$

The domain is divided into three rectangular regions. The velocity is zero at all solid walls and at infinite height $\frac{\partial u(\infty,z)}{\partial y} = 1$. At the gas-liquid interface (between regions I and III), the shear stress and velocity are matched:

$$u_{\mathrm{I}}(-f,z) = u_{\mathrm{III}}(-f,z), \tag{14}$$

$$\mu_{\mathrm{liquid}} \frac{\partial u_{\mathrm{I}}(-f,z)}{\partial y} = \mu_{\mathrm{gas}} \frac{\partial u_{\mathrm{III}}(-f,z)}{\partial y}. \tag{15}$$
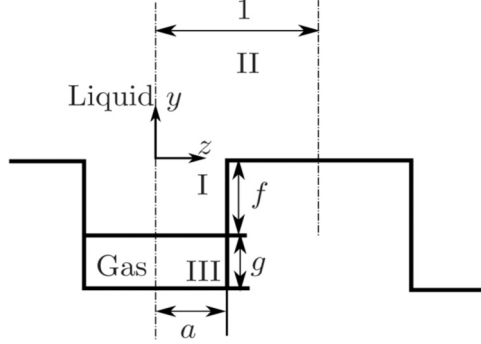
FIG. 7. The model problem and definitions of the geometric variables. Regions I and III are inside the groove filled with liquid and gas respectively. Region II is outside the groove, filled with liquid.

At the gas-liquid interface, we apply the approximate gas-liquid boundary condition:

$$\frac{\partial u_\text{I}(-f,z)}{\partial y} = \mu_r \frac{\partial u_\text{III}(-f,z)}{\partial y} = \mu_r \frac{u_s(z)}{g}, \tag{16}$$

from Eq. (12). This is valid when the gas flow inside the grooves is a Couette type flow or a pressure driven gas flow when the depth of the groove is small compared with the outside channel height, so that the velocity gradient can be obtained from linear approximation.

In region I, using separation of variables, $u_\text{I}(y,z) = v(y)w(z)$, and the approximate gas-liquid boundary condition above, the main assumption is that $w(z)$ is a linear function of the interface velocity at the interface between regions I and III:

$$u_s(z) = \alpha w(z). \tag{17}$$

Therefore, $\partial v(-b)/\partial y = \mu_r \alpha/g$. Then we obtain

$$u_\text{I} = \sum_{n=1}^{\infty} \frac{\alpha}{2} A_n \cos(\alpha_n z) \left[\left(\frac{\mu_r}{g\alpha_n} + 1 \right) e^{\alpha_n(f+y)} - \left(\frac{\mu_r}{g\alpha_n} - 1 \right) e^{-\alpha_n(f+y)} \right], \tag{18}$$

where $\alpha_n = (n - \frac{1}{2})\frac{\pi}{a}$. In region II, the general solution is

$$u_\text{II} = B_0 + y + \sum_{n=1}^{\infty} B_n \cos(\gamma_n z) e^{-\gamma_n y}, \tag{19}$$

where $\gamma_n = n\pi$.

The general solution for region III that satisfies the no-slip condition on the walls and symmetry is

$$u_\text{III} = \sum_{n=1}^{\infty} C_n \cos(\alpha_n z)[-e^{\alpha_n(y+2f+2g)} + e^{-\alpha_n y}]. \tag{20}$$

By satisfying Eq. (17) at the interface we get

$$\alpha A_n = C_n[-e^{\alpha_n(f+2g)} + e^{\alpha_n f}]. \tag{21}$$

At the boundary between regions I and II, u_I and u_II are matched by

$$u_\text{II} = \begin{cases} u_\text{I}, & 0 \leqslant z < a, \\ 0, & a < z \leqslant 1; \end{cases} \tag{22}$$

$$\frac{\partial u_\text{I}(-f,z)}{\partial y} = \frac{\partial u_\text{II}(-f,z)}{\partial y}. \tag{23}$$

TABLE II. Convergence of B_0, $a = 0.6$.

$f, g \backslash M$	5	10	15	20	25	30	35	40	45
1.25, 1.125	0.1319	0.1301	0.1307	0.1305	0.1306	0.1305	0.1306	0.1306	0.1306
0.25, 0.125	0.1289	0.1272	0.1278	0.1275	0.1277	0.1276	0.1277	0.1276	0.1277

Integrating Eq. (22) from 0 to 1 yields

$$B_0 = -\sum_{n=1}^{\infty} \frac{1}{2} C_n \frac{(-1)^n}{\alpha_n} [-e^{\alpha_n(f+2g)} + e^{\alpha_n f}] \left[\left(\frac{\mu_r}{g\alpha_n} + 1 \right) e^{\alpha_n f} - \left(\frac{\mu_r}{g\alpha_n} - 1 \right) e^{-\alpha_n f} \right]. \qquad (24)$$

Multiplying Eq. (22) by $\cos(\gamma_m z)$ and then integrating yields

$$B_m = \sum_{n=1}^{\infty} C_n L_{mn} [-e^{\alpha_n(f+2g)} + e^{\alpha_n f}] \left[\left(\frac{\mu_r}{g\alpha_n} + 1 \right) e^{\alpha_n f} - \left(\frac{\mu_r}{g\alpha_n} - 1 \right) e^{-\alpha_n f} \right], \qquad (25)$$

where

$$L_{mn} = \frac{\sin[\pi(ma + n - 0.5)]}{2\pi[m + (n - 0.5)/a]} + \frac{\sin[\pi(ma - n + 0.5)]}{2\pi[m - (n - 0.5)/a]}. \qquad (26)$$

Multiplying Eq. (23) by $\cos(\alpha_m z)$ and integrating from 0 to a gives

$$\sum_{n=1}^{\infty} -B_n L_{nm} \gamma_n - \frac{(-1)^m}{\alpha_m} = \frac{a}{4} C_m \alpha_m [-e^{\alpha_m(f+2g)} + e^{\alpha_m f}]$$

$$\times \left[\left(\frac{\mu_r}{g\alpha_m} + 1 \right) e^{\alpha_m f} + \left(\frac{\mu_r}{g\alpha_m} - 1 \right) e^{-\alpha_m f} \right]. \qquad (27)$$

B_m is truncated to M terms and A_n is truncated to $N = Int[aM]$ terms. Solving Eqs. (25) and (27) as a system of equations, we can solve for the mean slip velocity B_0 from Eq. (24). Table II shows the convergence of B_0 with respect to M, with two sets of f and g.

B. Results

The drag reduction originally predicted in [14] is based on constant pressure drop:

$$\mathrm{DR}_{\mathrm{ZS,CPD}} = \frac{Q_{\mathrm{no-slip}} - Q_{\mathrm{SHS}}}{Q_{\mathrm{no-slip}}} = 3 \left(1 - \frac{B_1}{B} \right), \qquad (28)$$

where $B_1 = \frac{K(k_1)}{K'(k_1)} \frac{2H}{w}$, $B = \frac{w+d}{w}$. For a constant flow rate, the drag reduction is defined by Eq. (9) and the theoretical solution by [14] can be converted to

$$\mathrm{DR}_{\mathrm{ZS,CFR}} = \frac{3(B - B_1)}{4B - 3B_1}, \qquad (29)$$

where the subscripts "CPD" and "CFR" denote constant pressure drop and constant flow rate respectively. Using the partial slip concept expressed in Eq. (12), with the B_0 derived in Eq. (24), the DR in a channel flow with grooved wall in one side can be solved analytically:

$$\mathrm{DR} = \frac{3\zeta}{4\zeta + 1}, \qquad (30)$$

where $\zeta = B_0(w + d)/(2H)$. Figure 8 compares the analytical drag reductions predicted by Eq. (30) and DNS results of cases F7–F25 and I7–I25 in Table I with the approximate boundary condition given by Eq. (12). The modeled simulations agree with multiphase VOF simulations. Also, it shows
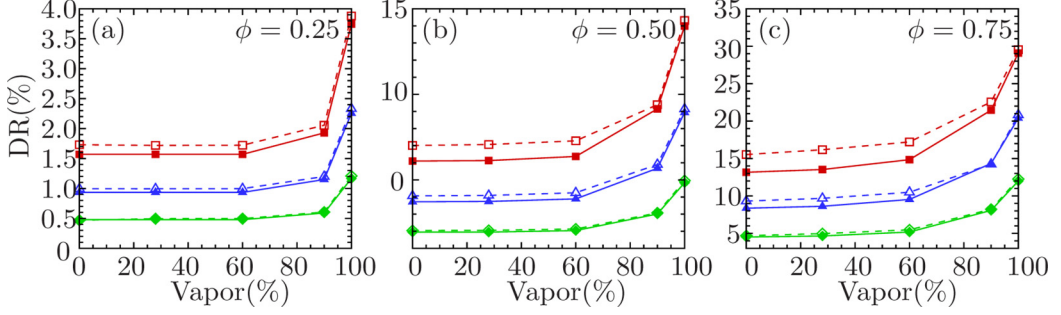
FIG. 8. Drag reduction comparison. The open symbols represent the DNS result; the solid symbols are predicted by the analytical solution from Eq. (30). The black dots are VOF simulations results. (a) Coverage ratio $\phi = 0.25$. (b) $\phi = 0.5$. (c) $\phi = 0.25$. –□–, case I7; –△–, case I12; –◇–, case I25.

good agreement between the analytical solution and the DNS results for cases F12, F25, I12, and I25, whose size of the texture is relatively small compared to the channel height, consistent with the assumption. For case I7, The deviation is large when $\phi = 0.75$ or when the channel height is comparable to the groove.

The effective slip length b_{eff} for a pipe flow with periodic no-slip or no-shear slots was derived in Lauga and Stone [15] using bulk quantities such as flow rate and pressure drop. For a plane channel flow, we obtain

$$b_{\text{eff}} = -\frac{12\frac{QH}{W} - 1}{12\frac{QH}{W} - 4}, \tag{31}$$

where all lengths are normalized by the channel height H, the velocities are normalized by KH^2/μ, and Q is the nondimensionalized volume flow rate.

Using the expression for Q in [13], Eq. (31) yields the zero-shear model effective slip length:

$$b_{\text{eff-ZS}} = \frac{B}{B_1} - 1. \tag{32}$$

From Eq. (29):

$$\text{DR}_{\text{ZS,CFR}} = \frac{3b_{\text{eff-ZS}}}{4b_{\text{eff-ZS}} + 1}. \tag{33}$$

Note that the drag reduction of a CPD case can be written as $\text{DR}_{\text{ZS,CPD}} = 3[1 - 1/(1 + b_{\text{eff-ZS}})]$. In [48], the drag reduction in a Couette flow between two surfaces of distance h with a slip length δ on one surface has a similar form: $\text{DR} = 1 - 1/(1 + \delta/h)$, where δ/h can be seen as the effective slip length in a Couette flow.

Comparing to Eq. (33), we observe that

$$b_{\text{eff}} = \zeta. \tag{34}$$

In the same manner as the definition of the effective slip length, the effective slip velocity u_{eff} can be defined as

$$u_{\text{eff}} = \frac{2QH}{W} - \frac{1}{6}. \tag{35}$$

And the analytical solution of the effective slip velocity for the zero-shear model is

$$u_{\text{eff-ZS}} = \frac{1}{2}\left(1 - \frac{B_1}{B}\right). \tag{36}$$
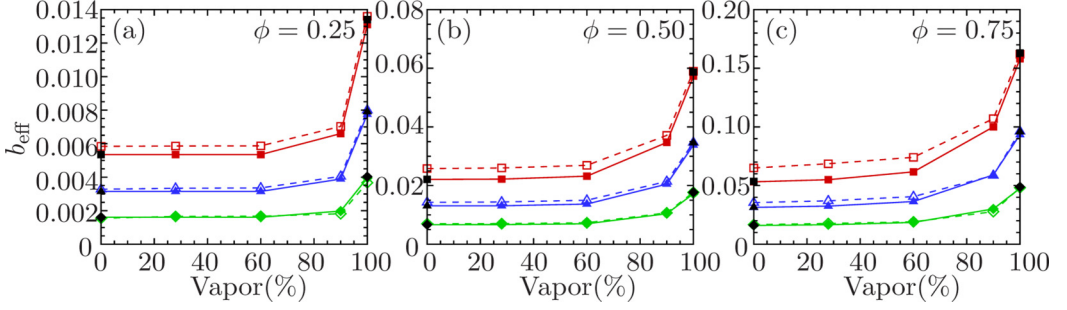
FIG. 9. Effective slip lengths comparison. The open symbols stand for the DNS result; the solid colored ones are from the analytical solution of Eq. (34); the black dots are VOF simulations results; the purple symbols are predicted by Eqs. (38) and (39). –□–, case I7; –△–, case I12; –◇–, case I25.

Written in terms of the analytical solution obtained, the effective slip velocity is

$$u_{\text{eff}} = \frac{\zeta}{2(\zeta + 1)}. \tag{37}$$

Figures 9 and 10 compare the DNS results with Eqs. (34) and (37) and VOF simulations respectively. Similar to the plots of drag reduction, the solution performs best when the size of the groove is small compared to the channel.

C. Scaling law of the drag reduction

To use Eq. (33) as a scaling law, one must know b_{eff} *a priori*. A theoretical prediction for b_{eff} is needed for three scenarios: (i) fully wetted grooved surface; (ii) partially wetted grooved surface; and (iii) grooves filled with gas.

When the depth of the fully wetted groove is large enough, which is true for the models in this paper, b_{eff} of the grooved surface is asymptotic to

$$b_{\text{eff}}^i = \frac{(w+d)}{2H\pi}[(1-\phi)\ln(1-\phi) + (1+\phi)\ln(1+\phi)], \tag{38}$$

which has been solved in [49] using the conformal mapping method and validated by Wang [38] for all $f \geqslant 2$ in the notation of this paper. The superscript $^i, ^{ii}, ^{iii}$ represents the scenarios itemized above. The b_{eff}^i for all the fully wetted simulations F7–F25 and all the flat interface simulations
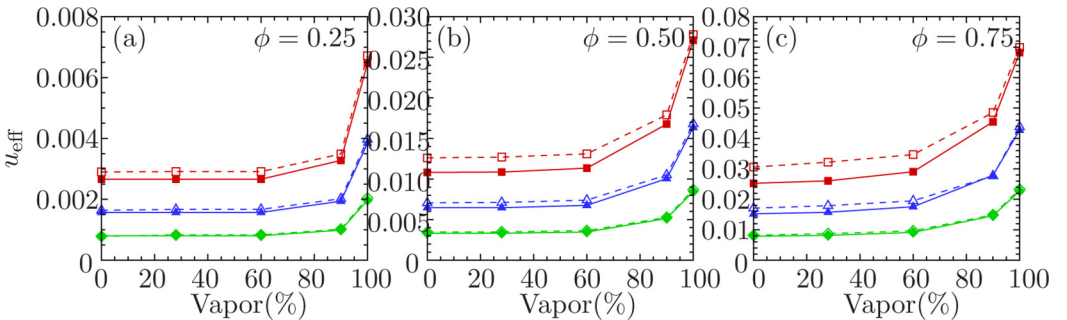

FIG. 10. Effective slip velocities comparison. The open symbols stand for the DNS result; the solid ones are from the analytical solution derived in this paper. The black dots are VOF simulations results. –□–, case I7; –△–, case I12; –◇–, case I25.

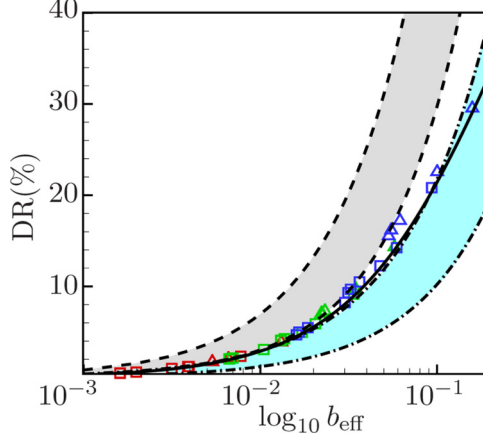FIG. 11. DR scales with b_{eff}. Solid line: Eq. (33); red: $\phi = 0.25$; green: $\phi = 0.5$; blue: $\phi = 0.75$; $\triangle$: cases F7 and I7; $\square$: cases F12 and I12; $\diamondsuit$: cases F25 and I25; blue shaded area: prediction by [38]; gray shaded area: prediction by [40].

I7–I25 are computed and plotted against the DR results in Fig. 11 as the gray shaded area. Note that since b_{eff}^i is not a function of the gas height, the results do not fall onto one line.

When the surface has zero-shear boundary condition, the exact expression for b_{eff} in [40] can be converted to be

$$b_{\text{eff}}^{iii} = \frac{-(w+d)}{H\pi} \ln \left[\cos \left(\frac{\pi}{2} \phi \right) \right]. \tag{39}$$

Similarly, the b_{eff}^{iii} for each simulation result is computed; the b_{eff}^{iii} − DR results are plotted in Fig. 11 as the blue shaded area. Again, because b_{eff}^{iii} is independent of the gas height, the results do not collapse.

Taking into account those two extreme conditions, b_{eff}^{ii} is a function of the groove geometry (w,d,b,H) and the shear rate of the interface (approximated by μ_r, h). The expression for b_{eff}^{ii} is

$$b_{\text{eff}}^{ii} = \frac{(w+d)}{2H} B_0, \tag{40}$$

where B_0 is from Eq. (24). b_{eff}^{ii} − DR relations from fully wetted and flat interface results are presented in Fig. 11 as symbols. The solid line is the prediction by Eq. (33). The figure shows that DR satisfies the scaling with respect to b_{eff}^{ii} derived in Eq. (40). The drag reductions DR of all the fully wetted grooved cases and all the flat interface cases, plotted against b_{eff}, collapse onto a single line. To conclude, Eq. (38) can only predict the b_{eff} of scenario (i); Eq. (39) can only predict scenario (iii); however, the analytical solution in this paper bridges the gap between these two scenarios. Figure 11 shows that our solution performs well over the full range of the gas portion.

D. A first order approximation using analytical solution

In [21], the relation between the effective slip length and the friction factor–Reynolds number product is

$$b_{\text{eff}} = 2 \left(\frac{8}{f\text{Re}} - \frac{1}{12} \right). \tag{41}$$

In this section, the analytical solution is examined with the experimental data in [21] by estimating a 16% liquid penetration and the interface being flat. Figure 12 shows that the analytical solution agrees
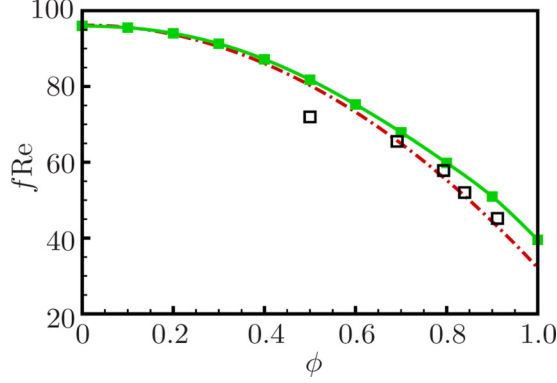
FIG. 12. Comparison of $f\mathrm{Re}$ with varying groove fractions ϕ. ■ analytical solution with 16% liquid penetration; □ experimental results by Maynes *et al.* [21]; ·— VOF simulation of flat interface with 16% liquid penetration.

with experiment data, especially when the coverage ratio is small. However, this approximation using the gas to liquid fraction inside the groove is strictly valid only when the channel height is large relative to the penetration, or when the contact angle is low so that the interface can be assumed to be flat.

IV. A NOTE ON INTERFACE CURVATURE

A. Predicting meniscus shape

Interface curvature can be modeled using the Young-Laplace equation:

$$\Delta p = \sigma \nabla \cdot \mathbf{n}, \tag{42}$$

where Δp is the pressure difference across the interface, σ is the gas-liquid surface tension, and $\mathbf{n}$ is the local normal. Assuming Δp to be constant along the interface, the interface shape for a groove is

$$F_{zz} = \xi \left(1 + F_z^2\right)^{3/2}, \tag{43}$$

where $\xi = \Delta p/\sigma$. A three-dimensional (3D) expression is given in [50]. Integrating Eq. (43) twice with the boundary conditions $F(\pm\frac{w}{2}) = 0, F_z(0) = 0$ yields the interface shape:

$$F(z) = -\frac{\sqrt{1 - \xi^2 z^2}}{\xi} + \frac{\sqrt{1 - \xi^2 w^2/4}}{\xi}. \tag{44}$$

Figure 13(b) shows the interface shapes for varying pressure difference. As the pressure difference increases, the interface penetrates towards the bottom of the groove and contact angle increases. VOF simulations of the same configuration were performed and compared to the results of the Young-Laplace equation; good agreement was observed [Fig. 13(c)].

B. Wetting: failure

The slope of the interface is

$$\eta = F_z = \tan(\theta - \pi/2), \tag{45}$$

therefore

$$\xi = -\frac{\eta}{(w/2)\sqrt{1 + \eta^2}} = \frac{2\cos\theta}{w}, \tag{46}$$

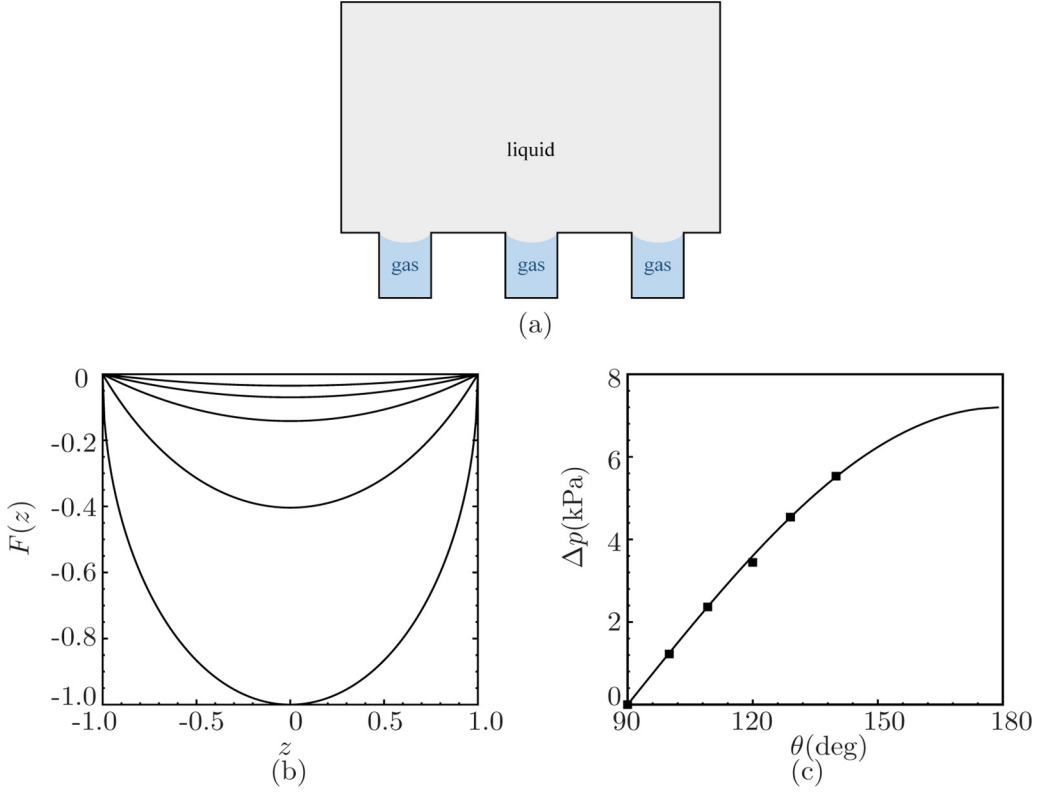which is similar to Eq. (1) from [36] when $\phi_g \approx \phi = w/(w + d)$.

FIG. 13. (a) Schematic diagram of the meniscus interface. (b) The shape of the gas-liquid interface changes with increasing pressure difference. From top to bottom: $\Delta p = 500, 1000, 2000, 5000, 7200$ Pa, from top to bottom. Unit: 10 μm (c) Contact angle θ vs Δp. The solid line represents the analytical solution. The symbols are VOF results.

A critical pressure difference Δp_{cr} can be defined as the pressure difference across the meniscus when contact angle $\theta = \pi$, provided that the groove is deep enough so that the interface does not touch the bottom first. The slope of the interface at $z = w/2$,

$$\lim_{\eta \to -\infty} \xi = \frac{2\cos(\pi)}{w} = \frac{2}{w}. \tag{47}$$

The critical pressure difference which quantifies failure due to wetting on the sides is

$$\Delta p_{cr} = \frac{2\sigma}{w}. \tag{48}$$

In this paper, for case F7 with $\phi = 0.5$, $\sigma = 7.2E - 2$ N/m for water at 20 °C, $\Delta p_{cr} = 7.2$ kPa.

C. Results

Simulations are performed to study the effect of the interface curvature in the grooved channel using both the VOF method and DNS of the liquid region alone, modeling the curved interface using Eq. (43). The modeled simulations used the approximate boundary condition Eq. (12) at the curved interface, whose height varies across the span of the groove. Figure 14 shows the variation in drag reduction with respect to contact angle θ and pressure difference Δp. Good agreement is observed between the VOF calculations and the calculations with the approximate boundary condition. Intriguingly, drag reduction initially increases with increasing Δp and θ following which
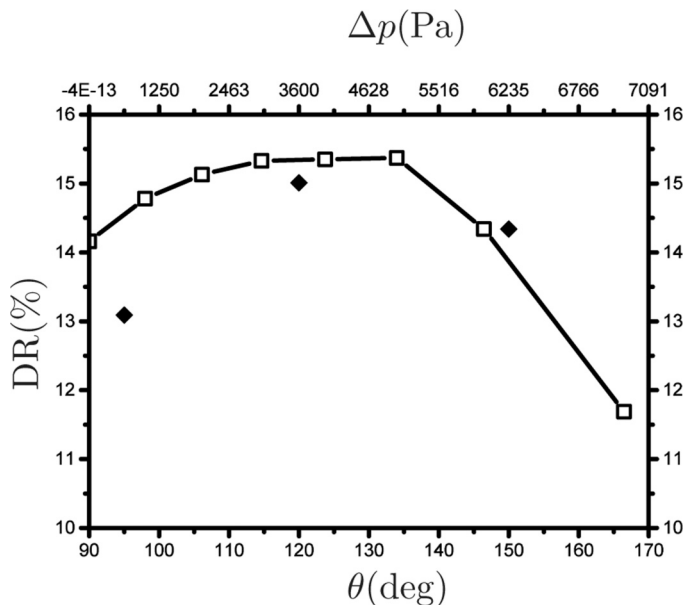
FIG. 14. Variation of drag reduction with contact angle θ and pressure difference Δp. (Open symbols are approximate boundary condition with meniscus shape simulations; solid symbols are VOF simulations).

it decreases. Such a trend is also observed in [22,27,28]. This behavior is due to the competing effects of interface area and height of the interface from the no-slip wall. The large reductions in drag obtained for $\Delta p < 5$ kPa results from the increase in the surface area over which larger slip velocities occur. For larger Δp, the interface approaches the bottom of the groove where the gas layer is thin, which results in the slip velocity decreasing and therefore the total shear stress is greater on the interface than that on an interface with lower Δp.

V. SUMMARY

Multiphase, feature-resolved simulations have been performed to study the factors that contribute to the drag reduction effect of SHSs: interface shear rate and the shape of the gas-liquid interface. First, VOF simulation results confirmed that the gas flow behavior inside the groove has an effect on drag reduction but the liquid penetration into the grooves is more significant. Next, an analytical solution of the shear flow over longitudinal grooves with coupled gas-liquid interface has been derived and validated with simulations using approximate gas-liquid boundary condition and VOF simulations. A scaling law of the drag reduction with respect to effective slip length has been obtained from the analytical solution. The solution can also be extended to liquid-infused surfaces. Consider for example two of the liquid conditions in the experiment of [29], $\mu_r = 1/2.7$ and 30, and the geometric parameters of case I7 with the grooves filled with a second fluid; the analytical solutions predict the drag reduction to be 9.50% and 0.35% respectively. Lastly, the shape of the interface has been examined by prescribing the location of the interface with the Young-Laplace equation and applying the approximate boundary condition. A series of physically representative meniscal interfaces which provided spanwise varying gas height in the groove have been simulated. For the meniscal cases, the drag reduction does not behave monotonically but peaks at a certain meniscal interface and then drops dramatically. This result can be explained as a compromise between the gas-liquid contact area and the shear stress on the gas-liquid interface. When liquid penetrates into the groove, the interface area increases but the local gas is depressed, which increases the shear stress on the interface. This behavior is also confirmed by VOF simulations.

APPENDIX: ASYMPTOTIC ANALYSIS OF THE ANALYTICAL SOLUTION

By modifying the shear rate matching between regions I and II in the solution of [38], it is straightforward to analytically solve the Stokes shear flow over grooves filled with gas:

$$\frac{\partial u_{\mathrm{I}}(-b^w, z)}{\partial y} = \mu_r \frac{\partial u_{\mathrm{II}}(-b^w, z)}{\partial y}. \tag{A1}$$

Here the superscript "w" is used to represent Wang's notation. b^w is the depth of the groove normalized by $(w + d)/2$. The expression for B_0 and B_m remain the same (see [38] for detailed solution) and the matrix integrated from Eq. (A1) becomes

$$\sum_{n=1}^{\infty} -B_n^w L_{nm} \gamma_n - \frac{(-1)^m}{\alpha_m} = \mu_r \frac{a}{2} A_m^w \alpha_m [1 + e^{-2\alpha_m b^w}]. \tag{A2}$$

Moreover, the fully wetted solution by Wang [38] can be recovered from the partial slip solution. When gas escapes from the liquid, $g = 0$, $f = b^w$, $\mu_r = 1$. Taking the limit of the right hand side (RHS) of Eq. (27),

$$\lim_{g \to 0} \mathrm{RHS} = \lim_{g \to 0} \frac{a}{4} C_m \alpha_m [-e^{\alpha_m(b^w + 2g)} + e^{\alpha_m b^w}] \left[\left(\frac{\mu_r}{g\alpha_m} + 1 \right) e^{\alpha_m b^w} + \left(\frac{\mu_r}{g\alpha_m} - 1 \right) e^{-\alpha_m b^w} \right]$$

$$= \frac{a}{2} C_m (-e^{2\alpha_m b^w}) \alpha_m [1 + e^{-2\alpha_m b^w}]. \tag{A3}$$

Comparing to the solution for fully wetted grooves: $C_m(-e^{2\alpha_m b}) = A_m^w$.

Taking the limit of Eq. (24) and applying L'Hopital's rule, and substituting C_m,

$$\lim_{g \to 0} B_0 = \lim_{g \to 0} -\sum_{n=1}^{\infty} \frac{1}{2} C_n \frac{(-1)^n}{\alpha_n} [-e^{\alpha_n(f + 2g)} + e^{\alpha_n f}] \left[\left(\frac{\mu_r}{g\alpha_n} + 1 \right) e^{\alpha_n f} - \left(\frac{\mu_r}{g\alpha_n} - 1 \right) e^{-\alpha_n f} \right]$$

$$= -\sum_{n=1}^{\infty} \frac{(-1)^n}{\alpha_n} A_n^w (1 - e^{-2\alpha_n b^w}). \tag{A4}$$

Similar is B_m from Eq. (25):

$$\lim_{g \to 0} B_m = \lim_{g \to 0} \sum_{n=1}^{\infty} C_n L_{mn} [-e^{\alpha_n(b^w + 2g)} + e^{\alpha_n b^w}] \left[\left(\frac{\mu_r}{g\alpha_n} + 1 \right) e^{\alpha_n b^w} - \left(\frac{\mu_r}{g\alpha_n} - 1 \right) e^{-\alpha_n b^w} \right]$$

$$= 2 \sum_{n=1}^{\infty} A_n^w L_{mn} (1 - e^{-2\alpha_n b^w}). \tag{A5}$$

Thus, the solution in [38] for fully wetted grooves is recovered from the partial-slip solution. Also, the solution for fully wetted grooves can be converted to full-gas solution with minor adjustments, as is shown in Eq. (A2).

[1] A. B. D. Cassie and S. Baxter, Wettability of porous surfaces, Trans. Faraday Soc. **40**, 546 (1944).
[2] R. S. Voronov, D. V. Papavassiliou, and L. L. Lee, Review of fluid slip over superhydrophobic surfaces and its dependence on the contact angle, Ind. Eng. Chem. Res. **47**, 2455 (2008).
[3] D. Quéré, Wetting and roughness, Annu. Rev. Mater. Res. **38**, 71 (2008).
[4] J. P. Rothstein, Slip on superhydrophobic surfaces, Annu. Rev. Fluid Mech. **42**, 89 (2010).
[5] K. B. Golovin, J. W. Gose, M. Perlin, S. L. Ceccio, and A. Tuteja, Bioinspired surfaces for turbulent drag reduction, Philos. Trans. R. Soc. London, A **374**, 20160189 (2016).
[6] M. B. Martell, J. B. Perot, and J. P. Rothstein, Direct numerical simulations of turbulent flows over superhydrophobic surfaces, J. Fluid Mech. **620**, 31 (2009).
[7] M. A. Samaha, H. V. Tafreshi, and M. Gad-el Hak, Modeling drag reduction and meniscus stability of superhydrophobic surfaces comprised of random roughness, Phys. Fluids **23**, 012001 (2011).
[8] H. Park, H. Park, and J. Kim, A numerical study of the effects of superhydrophobic surface on skin-friction drag in turbulent channel flow, Phys. Fluids **25**, 110815 (2013).
[9] T. O. Jelly, S. Y. Jung, and T. A. Zaki, Turbulence and skin friction modification in channel flow with streamwise-aligned superhydrophobic surface texture, Phys. Fluids **26**, 095102 (2014).
[10] S. Türk, G. Daschiel, A. Stroh, Y. Hasegawa, and B. Frohnapfel, Turbulent flow over superhydrophobic surfaces with streamwise grooves, J. Fluid Mech. **747**, 186 (2014).
[11] A. Rastegari and R. Akhavan, On the mechanism of turbulent drag reduction with super-hydrophobic surfaces, J. Fluid Mech. **773**, R4 (2015).
[12] J. Seo, R. García-Mayoral, and A. Mani, Pressure fluctuations and interfacial robustness in turbulent flows over superhydrophobic surfaces, J. Fluid Mech. **783**, 448 (2015).
[13] J. R. Philip, Flows satisfying mixed no-slip and no-shear conditions, Z. Angew. Math. Phys. **23**, 353 (1972).
[14] J. R. Philip, Integral properties of flows satisfying mixed no-slip and no-shear conditions, Z. Angew. Math. Phys. **23**, 960 (1972).
[15] E. Lauga and H. A. Stone, Effective slip in pressure-driven stokes flow, J. Fluid Mech. **489**, 55 (2003).
[16] C. Schönecker, T. Baier, and S. Hardt, Influence of the enclosed fluid on the flow over a microstructured surface in the cassie state, J. Fluid Mech. **740**, 168 (2014).
[17] A. V. Belyaev and O. I. Vinogradova, Effective slip in pressure-driven flow past super-hydrophobic stripes, J. Fluid Mech. **652**, 489 (2010).
[18] O. I. Vinogradova, Drainage of a thin liquid film confined between hydrophobic surfaces, Langmuir **11**, 2213 (1995).
[19] T. V. Nizkaya, E. S. Asmolov, and O. I. Vinogradova, Gas cushion model and hydrodynamic boundary conditions for superhydrophobic textures, Phys. Rev. E **90**, 043017 (2014).
[20] A. Busse, N. D. Sandham, G. McHale, and M. I. Newton, Change in drag, apparent slip and optimum air layer thickness for laminar flow over an idealised superhydrophobic surface, J. Fluid Mech. **727**, 488 (2013).
[21] D. Maynes, K. Jeffs, B. Woolford, and B. W. Webb, Laminar flow in a microchannel with hydrophobic surface patterned microribs oriented parallel to the flow direction, Phys. Fluids **19**, 093603 (2007).
[22] C. Cottin-Bizonne, J. L. Barrat, L. Bocquet, and É. Charlaix, Low-friction flows of liquid at nanopatterned interfaces, Nat. Mater. **2**, 237 (2003).
[23] M. Sbragaglia and A. Prosperetti, A note on the effective slip properties for microchannel flows with ultrahydrophobic surfaces, Phys. Fluids **19**, 043603 (2007).
[24] L. P. Wang, C. J. Teo, and B. C. Khoo, Effects of interface deformation on flow through microtubes containing superhydrophobic surfaces with longitudinal ribs and grooves, Microfluid. Nanofluid. **16**, 225 (2014).
[25] D. G. Crowdy, Analytical formulas for longitudinal slip lengths over unidirectional superhydrophobic surfaces with curved menisci, J. Fluid Mech. **791**, R7 (2016).
[26] A. M. J. Davis and E. Lauga, Geometric transition in friction for flow over a bubble mattress, Phys. Fluids **21**, 011701 (2009).

[27] C. Cottin-Bizonne, C. Barentin, É. Charlaix, L. Bocquet, and J. L. Barrat, Dynamics of simple liquids at heterogeneous surfaces: Molecular-dynamics simulations and hydrodynamic description, Eur. Phys. J. E **15**, 427 (2004).

[28] T. Biben and L. Joly, Wetting on Nanorough Surfaces, Phys. Rev. Lett. **100**, 186103 (2008).

[29] B. J. Rosenberg, T. Van Buren, M. K. Fu, and A. J. Smits, Turbulent drag reduction over air-and liquid-impregnated surfaces, Phys. Fluids **28**, 015103 (2016).

[30] Y. Liu, J. S. Wexler, C. Schönecker, and H. A. Stone, Effect of viscosity ratio on the shear-driven failure of liquid-infused surfaces, Phys. Rev. Fluids **1**, 074003 (2016).

[31] Y. Li, K. Alame, and K. Mahesh, Feature resolved simulations of turbulence over superhydrophobic surfaces, in *Proceedings of the 31st Symposium on Naval Hydrodynamics* (Monterey, CA, 2016).

[32] M. Reyssat, J. M. Yeomans, and D. Quéré, Impalement of fakir drops, Europhys. Lett. **81**, 26006 (2007).

[33] A. L. Dubov, K. Perez-Toralla, A. Letailleur, E. Barthel, and J. Teisseire, Superhydrophobic silica surfaces: fabrication and stability, J. Micromech. Microeng. **23**, 125013 (2013).

[34] C. W. Extrand, Criteria for ultralyophobic surfaces, Langmuir **20**, 5013 (2004).

[35] Q.-S. Zheng, Yang Yu, and Z.-H. Zhao, Effects of hydraulic pressure on the stability and transition of wetting modes of superhydrophobic surfaces, Langmuir **21**, 12207 (2005).

[36] C. Lee, C.-H. Choi, and C.-J. Kim, Structured Surfaces for a Giant Liquid Slip, Phys. Rev. Lett. **101**, 064501 (2008).

[37] K. Kamrin, M. Z. Bazant, and H. A. Stone, Effective slip boundary conditions for arbitrary periodic surfaces: the surface mobility tensor, J. Fluid Mech. **658**, 409 (2010).

[38] C. Y. Wang, Flow over a surface with parallel grooves, Phys. Fluids **15**, 1114 (2003).

[39] C.-O. Ng and C. Y. Wang, Stokes shear flow over a grating: implications for superhydrophobic slip, Phys. Fluids **21**, 013602 (2009).

[40] C. Ybert, C. Barentin, C. Cottin-Bizonne, P. Joseph, and L. Bocquet, Achieving large slip with superhydrophobic surfaces: Scaling laws for generic geometries, Phys. Fluids **19**, 123601 (2007).

[41] K. Mahesh, G. Constantinescu, and P. Moin, A numerical method for large-eddy simulation in complex geometries, J. Comput. Phys. **197**, 215 (2004).

[42] R. Scardovelli and S. Zaleski, Analytical relations connecting linear interfaces and volume fractions in rectangular grids, J. Comput. Phys. **164**, 228 (2000).

[43] J. U. Brackbill, D. B. Kothe, and C. Zemach, A continuum method for modeling surface tension, J. Comput. Phys. **100**, 335 (1992).

[44] S. J. Cummins, M. M. Francois, and D. B. Kothe, Estimating curvature from volume fractions, Comput. Struct. **83**, 425 (2005).

[45] B. R. Elbing, E. S. Winkel, K. A. Lay, S. L. Ceccio, D. R. Dowling, and M. Perlin, Bubble-induced skin-friction drag reduction and the abrupt transition to air-layer drag reduction, J. Fluid Mech. **612**, 201 (2008).

[46] R. J. Daniello, N. E. Waterhouse, and J. P. Rothstein, Drag reduction in turbulent flows over superhydrophobic surfaces, Phys. Fluids **21**, 085103 (2009).

[47] H. Park, G. Sun, and C. J. Kim, Superhydrophobic turbulent drag reduction as a function of surface grating parameters, J. Fluid Mech. **747**, 722 (2014).

[48] C. H. Choi and C. J. Kim, Large Slip of Aqueous Liquid Flow Over a Nanoengineered Superhydrophobic Surface, Phys. Rev. Lett. **96**, 066001 (2006).

[49] S. Richardson, A model for the boundary condition of a porous material. part 2, J. Fluid Mech. **49**, 327 (1971).

[50] B. Emami, H. V. Tafreshi, M. Gad-el Hak, and G. C. Tepper, Predicting shape and stability of air-water interface on superhydrophobic surfaces with randomly distributed, dissimilar posts, Appl. Phys. Lett. **98**, 203106 (2011).